

Deconvolution of ASCA X-ray data: I. Spectral-imaging method

D.A. White¹ & D.A. Buote^{1,2,3}

¹Institute of Astronomy, Madingley Road, Cambridge CB3 OHA. (E-mail: daw@ast.cam.ac.uk)

²UCO/Lick, University of California at Santa Cruz, Santa Cruz, CA95064, U.S.A.

³AXAF Fellow

Received ***; in original form ***

ABSTRACT

In this paper we describe a self-contained method for performing the spectral-imaging deconvolution of X-ray data on clusters of galaxies observed by the *ASCA* satellite. Spatially-resolved spectral studies of data from this satellite require such a correction because its optics redistribute photons over regions which are of comparable size to the angular scales of interest in clusters. This scattering is a function not only of spatial position but also energy. To perform a correction for these effects we employ Maximum-Likelihood deconvolution of the image (within energy bands of 1 keV) to determine the spatial redistribution, followed by a Monte-Carlo energy reassignment of photon energies with position to determine the spectral redistribution. We present tests on simulated cluster data, convolved with the various instrumental characteristics and the X-ray background, which show that our methodology can successfully recover a variety of intrinsic temperature profiles in typical observational circumstances. In Paper-II we apply our spectral-imaging deconvolution procedure to a large sample of galaxy clusters to determine temperature profiles, some of which will be used in subsequent mass determinations, presented in Paper-III.

Key words: methods: data analysis – methods: numerical – techniques: image processing – X-rays: galaxies – galaxies: intergalactic medium – galaxies: fundamental parameters – galaxies: cooling flows

1 INTRODUCTION

One of the most important goals in the X-ray study of clusters of galaxies is the determination of their mass properties. The radial distribution of the total gravitating mass in a cluster can be constrained by accurate spatially-resolved observations of the gas temperature and density, combined with the simple assumption of hydrostatic equilibrium. While the accurate determination of density profiles is well within the capabilities of previous instrumentation (*e.g.* *ROSAT*), accurate radial temperature profile constraints requires good spectral *and* spatial resolution.

The *ASCA* satellite has the spectral resolution required, but the spatial resolution provided by its nested foil mirrors is inadequate for the analysis of extended sources, such as galaxy clusters. The on-axis half-power diameter of the point-spread function (PSF), of approximately 3 arcmin, increases and becomes increasingly asymmetric with off-axis position. However, the essential problem with the PSF is that it varies with energy, such that scattering is more severe for harder photons. Consequently, if no correction is applied to an *ASCA* dataset then the determination of the spatially-resolved temperature characteristics of a cluster will be incorrect. For a truly isothermal cluster, the PSF will produce a temperature

profile which appears to rise with increasing radius from the cluster core (Takahashi et al. 1995).

Most of the results presented currently in the literature, that attempt to correct for the spatial and energy-dependent nature of the *ASCA* PSF, use a method created by Markevitch et al. (1996). Their procedure relies on having an accurate prescription for the emissivity profile of the cluster – usually a β -model fit obtained from a *ROSAT* surface-brightness profile. Simulated cluster photons are generated according to an initial guess for the cluster spectrum, and spatially distributed according to the emissivity profile. The photons are then convolved with the spatially-variable PSF in different energy bands, and the model cluster compared with the observational data. The source spectrum is then varied at different positions until the model and observational data are statistically consistent.

The advantage of their method is that the spatially-variable nature of the PSF is easily incorporated, while the disadvantages are that the results may be compromised by the applicability of the spectral model and the accuracy of the emissivity profile. The latter issue may be important because the *ROSAT* energy band (0.2 – 2 keV) is significantly different from that of *ASCA* [0.5 – 10 keV – although Markevitch et al. (1998) use 2 – 10 keV]. Therefore, there may be significant mismatch between the emissivity profile

2 D.A. White and D. Buote

described by *ROSAT* and that required for the *ASCA* data analysis, if the cluster exhibits spatial variations in temperature or other properties which affect the spectrum, *i.e.* a cooling flow cluster will have many temperature components and a probable variation in the column density across the cluster (although this has to be large to affect the spectrum above 2 keV).

Using the above method, Markevitch et al. (1998) (hereafter *MFSV*) and others [Markevitch et al. (1996); Sarazin, Wise, & Markevitch (1998); Donnelly et al. (1998); Henricksen & Markevitch (1996); Markevitch, Sarazin, & Irwin (1996); Markevitch & Vikhlinin (1997); Markevitch (1996)] have presented temperature profiles for many clusters of galaxies. In a particular *MFSV* analysed a sample of 30 objects and found that most of these clusters have temperature profiles that decline with radius, which they parameterised with an average polytropic index of $\gamma = 1.24^{+0.20}_{-0.12}$.

This index is close to, and consistent with at the 2σ boundary of their uncertainties, the convective instability limit of $\gamma \geq 5/3 = 1.67$. While convective instability may be expected in clusters which have been disturbed, this should not be the case for relaxed clusters. Indeed, because cooling flows should be disrupted in significant merger events they can be taken as an indicator of cluster relaxation (Buote & Tsai 1996 and Buote 1998). However, as *MFSV* themselves find that approximately 60 percent of their clusters contain a cooling flow, there is a inconsistency between the apparent proportion of relaxed clusters in their sample and the possibility that the sample is close to convective instability – as implied by their steep temperature gradients.

Additionally, the steep temperature gradients exacerbate the baryon problem in clusters (White et al. 1993; Briel, Henry, & Böhringer 1992; White & Fabian 1995) – *i.e.* the apparent discrepancy between the large relative fraction of the total mass in baryons (*i.e.* essentially that seen as X-ray emitting gas), and the fraction expected from the production of baryons during primordial nucleosynthesis in a flat ($\Omega_0 = 1$) Universe. Declining temperature gradients imply smaller total cluster masses than would be inferred from isothermal temperature profiles, (if the electron and ion temperatures are in equipartition, Ettori & Fabian 1998), thereby leading to even larger baryon fraction determinations.

Although Markevitch et al. themselves show that their average temperatures determinations agree well with those obtained from previous broad-beam satellites such as *Einstein*, *EXOSAT* and *Ginga*, the crucial question is whether the shape of their temperature profiles are correct. For this their supporting evidence relies mainly on the consistency of the temperature profiles from the different *ASCA* detectors. Markevitch & Vikhlinin (1997) have performed a comparison of *ASCA* results with *ROSAT* temperature profiles, and found reasonable agreement, but the *ROSAT* temperature determinations have rather large uncertainties.

There are a growing number of results published which use different methods. Many of these results (*i.e.* Ikebe et al. 1997: A780; Fujita et al. 1996: A399 and A401; Ezawa et al. 1997: AWM7; Ohashi et al. 1997: 3A0336+098, MKW3s, A1795 and PKS2354–35) have been compared with those from Markevitch et al. by Irwin, Bregman, & Evrard (1998). They highlighted the fact that many of these other authors determine that these clusters have isothermal temperature profiles, even in cases where Markevitch et al. find a clear decline. Irwin et al. also presented their own analysis of *ROSAT* colour profiles which showed that their clusters were generally consistent with isothermality. Most recently,

(Molendi et al. 1999) have presented Beppo-SAX results which show that A2319 is isothermal, although these authors are reluctant to claim any significant discrepancy with the Markevitch et al. results on the basis of this one observation.

Given the importance of generic temperature declines in clusters, and their contradiction with other results, it is essential that the *ASCA* data are analysed by independent means to check the *MFSV* results. Also, *ASCA* data currently still provide the best opportunity for the most accurate temperature profiles determinations for a large sample of clusters. Thus, we we have created our own ‘spectral-imaging’ deconvolution (*SID*) procedure. Our method is self-contained: it requires only *ASCA* observational data on the cluster, background, and the energy-dependent PSF. It does *not* require *ROSAT* constraints on the emissivity profile. Also, no assumption about the various components contributing to the source spectrum is required in order to perform the deconvolution, and our method is essentially non-parametric. The main assumption that we have made is that a spatially *invariant* PSF is sufficient for our purposes. This has been done for computational speed and for convenience (we use a third party image deconvolution routine – see Section 2.1), although the consequences of this assumption are tested for, and are shown to be acceptable.

Such tests are central to our methodology, in order that we may be confident in the validity of our results. Thus, we have tested our procedure on simulated clusters by subjecting them to the various instrumental and background effects that will occur in the practical application of the method to real GIS data. For example, we have investigated the effect of the position-dependent nature of the PSF, looked at the degradation in performance with decreasing signal-to-noise, and tested the procedures ability to recover a variety of intrinsic cluster temperature profiles.

In summary, this paper presents a spectral-imaging deconvolution method for practical use with *ASCA* data on clusters of galaxies. In Paper-II (White 1999a), we apply this method to a large sample of *ASCA* GIS cluster observations, and compare our results with the results from *MFSV*.

2 METHOD

Our procedure for the spectral-image deconvolution (*SID*) of *ASCA* data can be broadly divided into two sections: image deconvolution followed by spectral reassignment, as summarised by a flow-diagram of the method shown in Fig.1.

2.1 Image Deconvolution

The image deconvolution is performed in the Interactive Data Language (IDL) environment using a maximum-likelihood (M-L) procedure, distributed with the ASTRON^{*} library of contributed routines by W. Landsman. Although this procedure accounts for the effect of Poissionian noise in the image, it has two significant drawbacks: it assumes, (i) that the PSF is spatially invariant, and (ii) that the data are monochromatic.

The first issue of the spatial variance of the PSF is neglected,

* <http://idlastro.gsfc.nasa.gov/homepage.html>

as we will assume that the PSF appropriate to the position of the cluster in the detector image can be used for the whole image deconvolution. We argue that this is reasonable, on the basis that most of the photons we are interested in arise from the core of the cluster. However, the impact of this assumption is assessed in the test detailed in Section 4.5.2.

The monochromatic issue is dealt with by dividing the data according energy, and executing the deconvolution on the image for each energy band. This can not be done for the data in each individual PI (pulse invariant) channel, as the M-L deconvolution procedure requires more counts to work with than will be found within one PI channel, and the PSFs which are available in the *ASCA* calibration database (CALDB) at HEASARC (High-Energy Astrophysics Archive, Goddard Space Flight Center) are only supplied in 1 keV bandwidths from 1 to 10 keV.

Our methodology is to take the X-ray events from each cluster observation and divide them into broad spectral energy bands, corresponding to the energy ranges of the PSF images. We then construct images from the data events in each of these energy bands (Fig. 1 – steps D.1 and D.2) and then pass them, along with the appropriate point-spread function, to the image deconvolution procedure (step D.3). After 50 iterations the M-L procedure returns the deconvolved image for that energy band (step D.4). (The effect of varying the number of iterations is investigated in Section 4.5.)

These deconvolved images are then supplied to the spectral reassignment phase to determine the PI energy of events which will comprise the deconvolved dataset.

2.2 Spectral Re-assignment

From the M-L procedure we know the spatial probability distribution of photons in the deconvolved plane. We also know that the total number of counts are conserved between the convolved and deconvolved planes. Therefore, we can create a random set of positions and energies from the deconvolved image and the observed PI distribution. However, we do not know which event has which PI energy.

Instead of attempting to recover the individual PI information for each event we could have performed a colour analysis of the deconvolved surface-brightness profiles in each 1 keV energy band (approximately 85 PI channels). However, this would fail to utilise the superior spectral capabilities of *ASCA*, and would lead to a degeneracy in temperature and abundance determinations. Thus, we have endeavoured to maintain the spectral resolution of *ASCA* by finding a way of assigning energies to the events list created from the deconvolved images.

The obvious procedure would be to randomly assign an energy for each event using the overall spectral distribution of events within the 1 keV energy band, however this is not correct if there is spatial variation of the PI events over this energy band, as the following example illustrates. Consider two spatially distinct point sources within a single 1 keV energy band interval: one emitting 1.2 keV photons and the other 1.8 keV events. A random assignment of energies in this energy band, which does not take into account any spatial information, will result in each point source having half of the 1.2 keV photons and half of the 1.8 keV photons. If the same number of photons were detected from each source, they would both end up with an incorrect mean energy of 1.5 keV.

To make the correct reassignment we need to choose a ‘prior’ spatial distribution for the events within each 1 keV energy band. For this we use the M-L deconvolved image (while *MFSV* use the *ROSAT* data to obtain a higher spatial-resolution emissivity profile). We can then effectively ‘ray-trace’ events from this image through the telescope optics and determine the most likely association between events in the deconvolved and convolved planes. As we know the energies of each convolved event we then know the energy of the deconvolved event.

In our ray-tracing method we assume the PSF is invariant within each energy band. (We discuss the systematic bias that this can introduce into our results in Section 4.5.) For each PI channel we randomly generate the appropriate number of *source*-plane events from the deconvolved image (steps R.1 to R.3). We then use the PSF to scatter these events into the *image*-plane (step R.4). If any of these *image*-plane events correspond to the positions of an observed photon (for the PI energy in question), then we consider this ‘mapping’ to be successful (R.5). We do this until all the photons in the PI channel in question have been successfully mapped.

Having obtained the position and energy of a *source*-plane event we can store the information (R.6) and eliminate the appropriate photon from the observed event list. We continue the ray-tracing until all the observed events are accounted for (R.7). As the number of events to be reassigned declines, the probability of finding a successful mapping reduces. For efficiency we mask out parts of the PSF which can not provide a successful link between a *source*- and *image*-plane position. Each randomisation is thereby guaranteed a successful mapping and the computational efficiency is improved significantly.

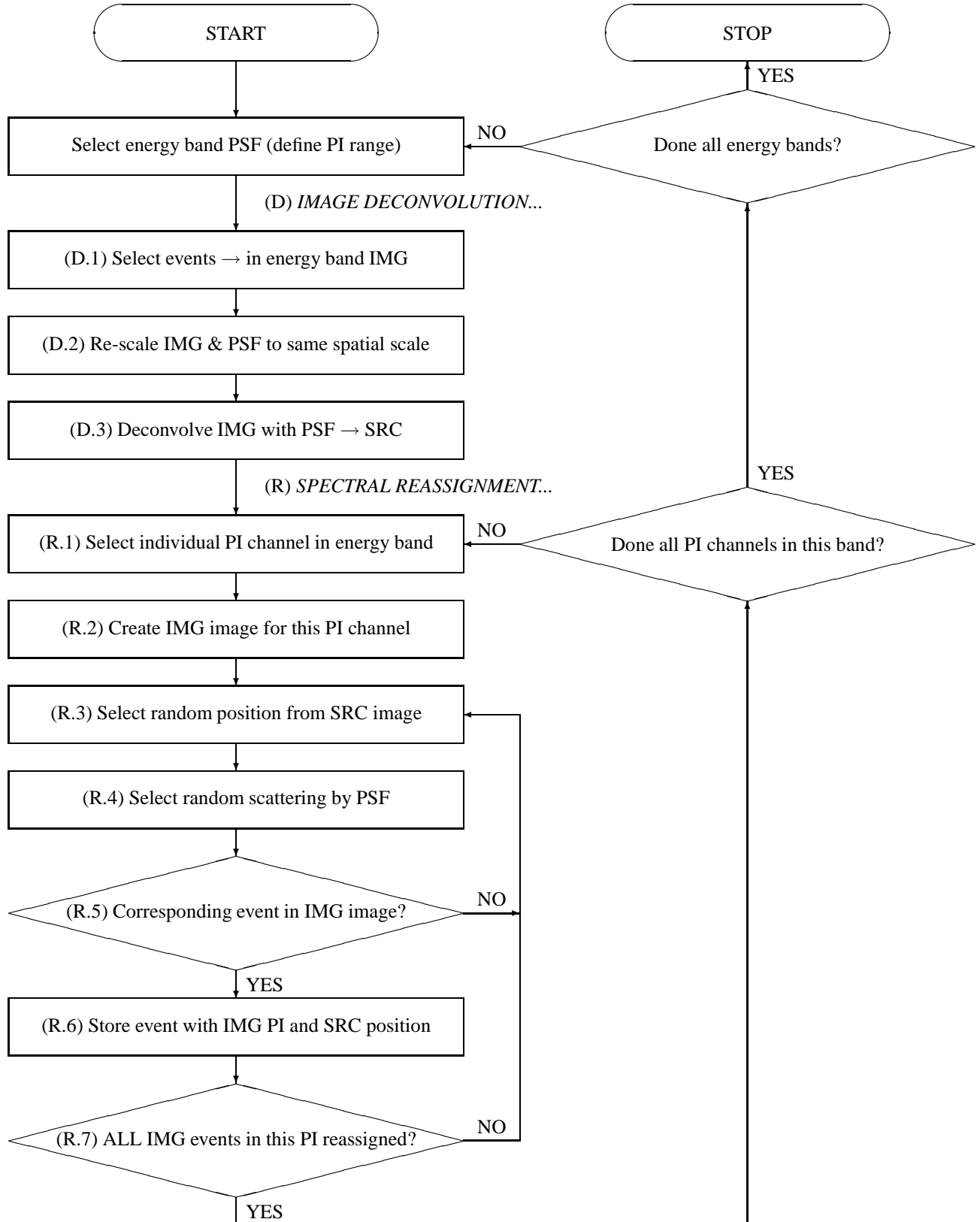
2.3 Practical Considerations

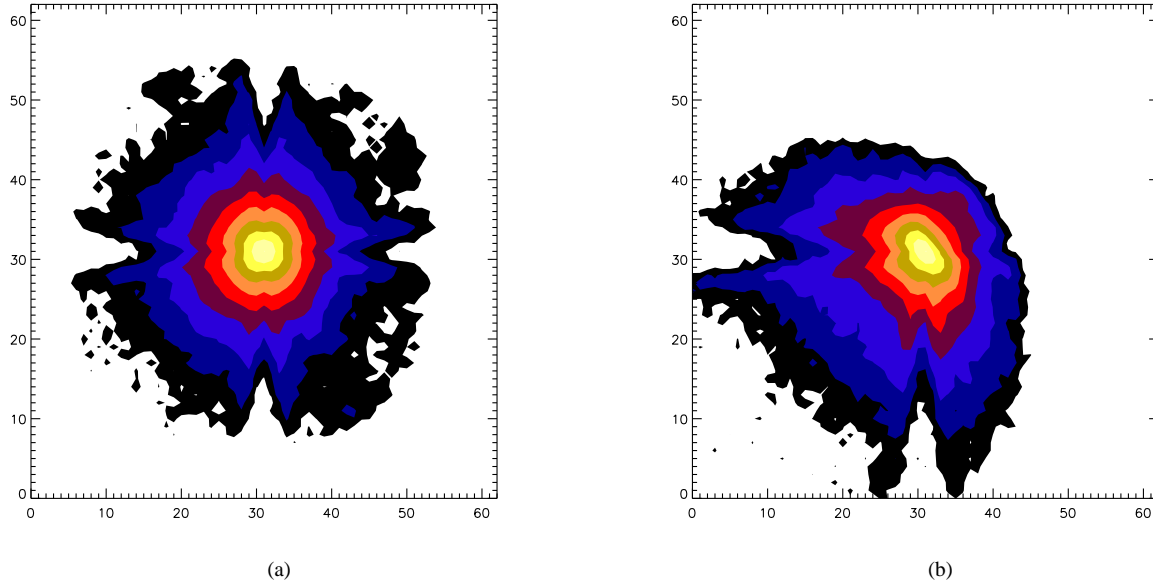
We have implemented our procedure in the Interactive Data Language (IDL) environment. The deconvolved events listings are written to standard (FITS) format files, which are then analysed using conventional X-ray data processing procedures (FTOOLS 4.2 and XSPEC 10.00 – see below). We currently only analyse GIS data as it has a larger field-of-view (FOV)[†] than the SIS – which allows us to determine cluster properties to larger radii. (The larger FOV also conserves more of the photons scattered to larger off-axis angles by the PSF. The SIS also has gaps between the CCDs, and the individual CCDs have differing instrumental gains.)

With the methodology we have defined above, there are various assumptions and complications which have to be assessed before we can be confident in applying it to real data. Firstly, we have noted, the M-L image deconvolution procedure only accepts a spatially invariant point-spread function, while the X-ray telescope (XRT) of *ASCA* exhibits a significant variation with position around the field of view (*e.g.* see Fig. 2). In the spectral reassignment we also assume that the PSF does not change significantly across each 1 keV energy band. Secondly, observational data also include contaminating events from cosmic X-ray sources, and from the X-ray detector itself. Finally, systematic effects introduced by the procedure have to be minimised.

[†] The usable area of the GIS is circular and ~ 40 arcmin in diameter, while the SIS is square and ~ 18 arcmin on a side.

Figure 1. Flowchart of the spectral-imaging deconvolution procedure. ‘SRC’ refers to the ‘source plane’ data (*i.e.* the actual data before it is affected by the satellite instrumentation) which we are attempting to recover, and ‘IMG’ refers to the ‘image plane’ data (*i.e.* the observed data after convolution *etc.*).



**Figure 2.**

In plots (a) and (b) we show (in logarithmic intensity) the combined XRT and GIS PSF (1 – 2 keV) at two extreme positions: 1.8 arcmin off-axis with a position-angle of 5° and 13 arcmin off-axis with a position-angle 40°, respectively. This highlights the change of the PSF with position in the detector image.

Dealing with the last of these points first, our experience has shown that a single realisation of the deconvolved data is subject to systematic effects. In particular, we noticed that the abundance profiles show abrupt variations which were clearly due to systematics in the procedure (the M-L image deconvolution). However, these can be reduced by repeating the *SID* procedure many times. Due to time constraints, we found that 10 repetitions was the maximum number we could deal with practically. To perform the Monte-Carlo procedure we randomise each input (convolved) dataset, and then process each deconvolved events list independently in separate spectral analyses. The spectral results are then combined to give the average profiles presented in the simulation results plots (this radial-profile averaging procedure is described in Paper-II). As the error bars in these plots are larger than the variations from bin-to-bin (and larger than the errors on either the original or convolved data) it is clear that the errors in the deconvolved profiles are dominated by systematic errors rather than statistical errors. However, the abundance profiles, in particular, are now much better behaved than found in any single realisation.

For the other two points listed above, we believe the only effective way to investigate the validity of our procedure, especially in circumstances typical of an *ASCA* observation, is to create simulated cluster datasets and then apply the various observational and systematic effects to see how well the original physical properties of the intracluster gas are recovered by the deconvolution procedure. In the description below, we indicate how we create these various simulations and how we assess the impact of these various contaminants in practical observational circumstances.

3 ANALYSIS

3.1 Generating Cluster Models

We generate the basic simulated cluster dataset from a radial density profile, parameterised by a standard β -model, and an isothermal temperature profile. The expected flux from each component (a second component is added to mimic a cooling flow cluster) of the intracluster medium (ICM) is determined by projecting the volume emissivity along the line-of-sight and convolving this with the spectral response of the detector. The distribution of counts in each PI detector channel is then obtained by randomly sampling the intrinsic cluster spectrum. This is repeated until the total observed flux is obtained for each thermal component. Similarly, the detected spatial position of each event is determined by random generation from the projected emissivity, followed by convolution with the spatial PSF. Note, the effect of vignetting is implicitly incorporated by our use of a spatially variable PSF to create the simulated datasets, as the normalisation of the PSF describes the efficiency of the detector at that position.

The cosmic background (from observations held at the *ASCA* CALDB at HEASARC) can also be included by adding in the expected number of background events from an observation of a blank area of real sky, and scaling for the relative exposure time of the simulated dataset. Because the background data are taken from actual observations of blank-sky fields these data are already convolved with the real spatially-variable PSF and include all the various sources of noise, such as the GIS calibration source, *e.g.* see Fig. 4(b).

The convolved simulated dataset, incorporating optional instrumental and background effects, is then supplied to our *SID* procedure, along with the PSFs. The PSFs in each 1 keV energy band are selected to most closely correspond to the position of the center of the cluster in the detector image. In the following section, we compare the results from the various tests which are designed to as-

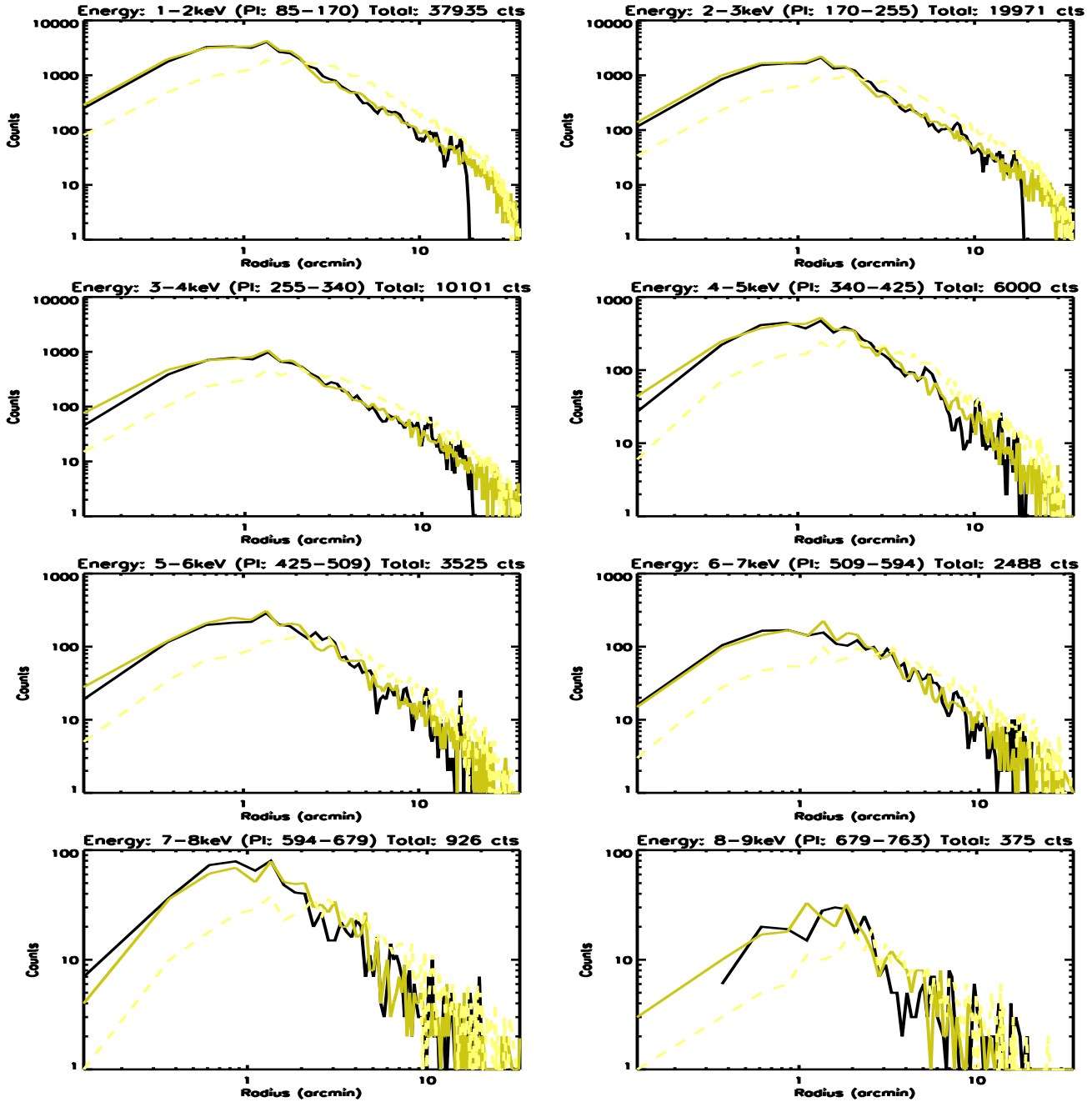


Figure 3.

This figure presents a comparison of the original (medium-dark, solid line), deconvolved (dark, solid line) and convolved (light, dashed line) surface-brightness profiles for the (TEST-NOBGD-30K) simulations with no background contamination. This enables a direct comparison to be made of how well the *SID* procedure recovers the true surface-brightness profiles in each energyband. Although the *SID* procedure introduces extra noise, the true surface-brightness profiles are clearly recovered well (the deconvolved data are truncated outside 20 arcmin), and are significantly better representations than the surface-brightness profiles from the convolved data, even in the higher-energy bands which have few counts.

sess the impact of the assumptions implicit in our method, and the various observational contaminants such as the X-ray background.

We judge the success of the *SID* procedure by its ability to recover the properties of the original simulated cluster, and to do this we perform a spatially-resolved spectral analysis on the original, convolved, and deconvolved events and then compare the results graphically. Although the correct recovery of the original temperature profiles by the *SID* procedure implicitly requires that the orig-

inal surface-brightness profiles are correctly recovered by the M-L deconvolution in each 1 keV energyband, this is explicitly shown in Fig. 3.

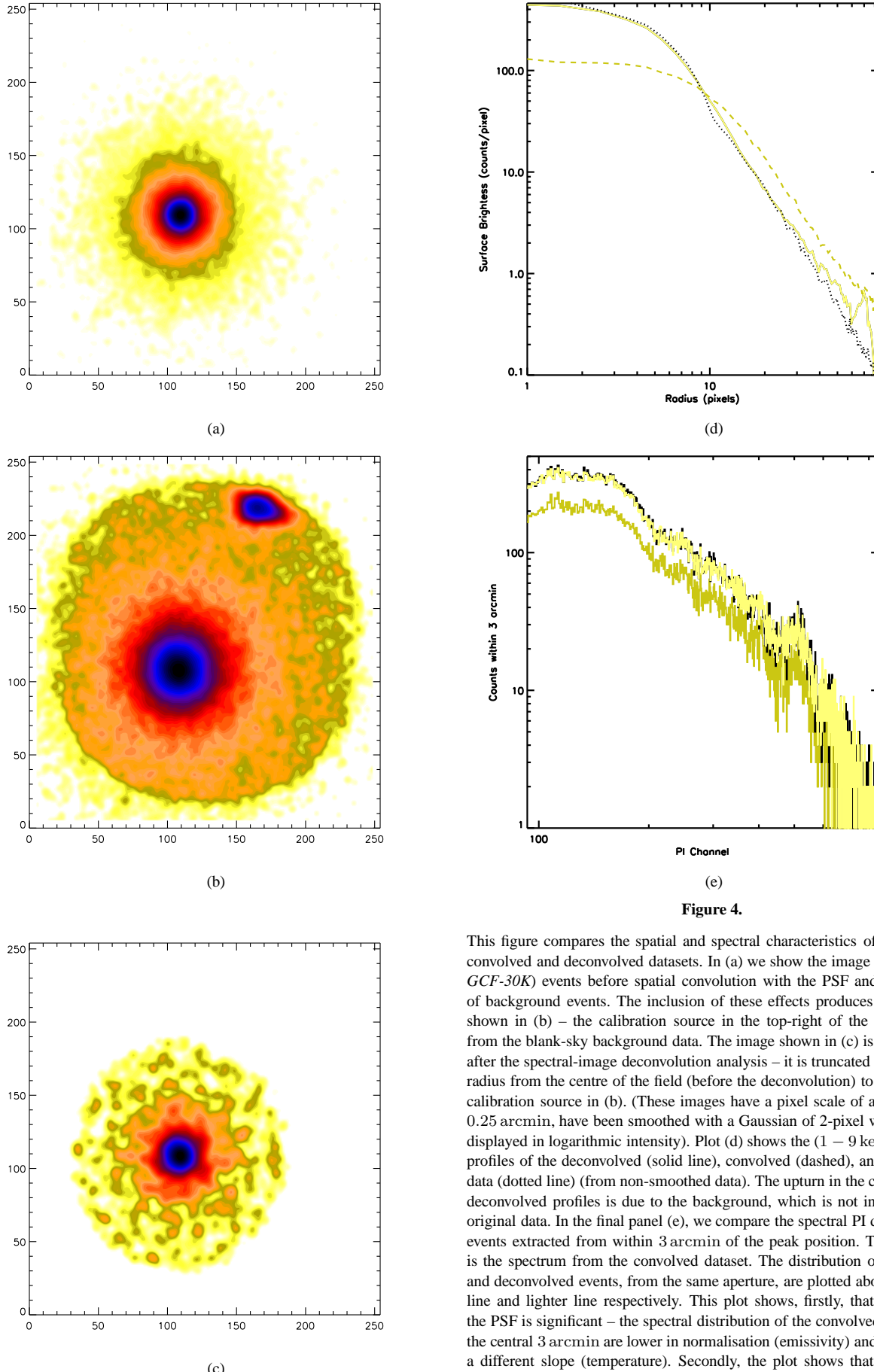


Figure 4.

This figure compares the spatial and spectral characteristics of the original, convolved and deconvolved datasets. In (a) we show the image of the (*TEST-GCF-30K*) events before spatial convolution with the PSF and the addition of background events. The inclusion of these effects produces in the image shown in (b) – the calibration source in the top-right of the image comes from the blank-sky background data. The image shown in (c) is that obtained after the spectral-image deconvolution analysis – it is truncated at 20 arcmin radius from the centre of the field (before the deconvolution) to eliminate the calibration source in (b). (These images have a pixel scale of approximately 0.25 arcmin, have been smoothed with a Gaussian of 2-pixel width, and are displayed in logarithmic intensity). Plot (d) shows the (1 – 9 keV) azimuthal profiles of the deconvolved (solid line), convolved (dashed), and the original data (dotted line) (from non-smoothed data). The upturn in the convolved and deconvolved profiles is due to the background, which is not included in the original data. In the final panel (e), we compare the spectral PI distribution of events extracted from within 3 arcmin of the peak position. The lower line is the spectrum from the convolved dataset. The distribution of the original and deconvolved events, from the same aperture, are plotted above as a black line and lighter line respectively. This plot shows, firstly, that the effect of the PSF is significant – the spectral distribution of the convolved events from the central 3 arcmin are lower in normalisation (emissivity) and also exhibits a different slope (temperature). Secondly, the plot shows that the spectral-

3.2 Spectral Analysis

The spectral analysis procedure which we employ is fairly standard. We start by defining annular regions of interest, centred on the peak of the X-ray emission, and then fit a spectral model to each of these regions and compare the results. The maximum radius allowed for any cluster extraction is 20 arcmin from the centre of the field of view (although the region of most practical interest will generally be within the inner 10 arcmin). This eliminates the gain uncertainties at the edge of the GIS detector and contamination from the calibration source. However, if the background has been incorporated the maximum radius is usually reduced to the radius where the background-subtracted surface-brightness profile remains positive. The background spectrum is extracted from the blank sky observations using the same spatial regions defined by the cluster data. In this way any gross position-dependent detector variations, such as instrument gain, should cancel out.

After defining each annular region, such that each annulus contains a certain fraction of the total (if applicable – background subtracted) counts (0.1^{\dagger} – which gives a theoretical maximum of 10 radial bins; see Paper-II for details on the methodology), we extract events using FTOOLS 4.2. This is done for both the source and background spectra. These spectra, together with the ancillary response matrix (*i.e.* ARF file; determined using ASCAARF), are passed to the XSPEC 10.00 spectral analysis package (Arnaud 1996), and fitted with the chosen spectral model. We note that, until this point, no assumption has been made about the intrinsic cluster spectrum, and any chosen model can be fitted to the deconvolved data – contrary to the procedure used by *MFSV* which requires a spectral model to be defined as an integral part of the deconvolution.

In this analysis we fit a single temperature plasma emission model[§] – regardless of whether the simulated data were created with two thermal components. This means that we are not using the correct model for the data, but for the simulations this is not important. The crucial fact is whether we recover the same results from the deconvolved data as from the original data using the same spectral model. Thus, in the following results we are looking for good agreement between the spectral fits to the deconvolved and original datasets (*i.e.* simulated data which have been convolved with the spectral response, but not the spatial PSF). (We do note, however, that our lack of a cooling flow component, and particularly the excess absorption, in the fitted model is largely responsible for the radial increase in metallicities in the cooling flow simulations, which is not apparent in the single thermal component models.)

Finally, we note that if background contamination is included in the test it is also applied to the convolved data (and thereby the deconvolved data), but not the original data. Thus, no background subtraction is performed in the spectral analysis of the original dataset. This also means that (except in the test which has no back-

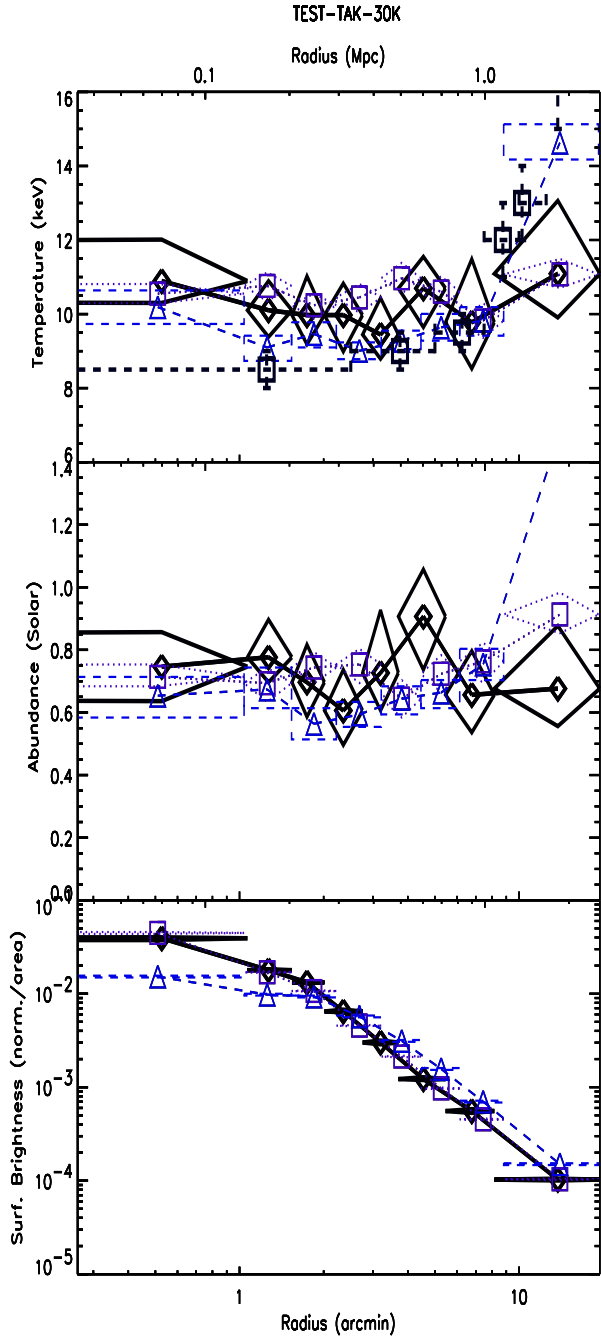


Figure 5. This figure shows the effect of the PSF on isothermal cluster data (the underlying original isothermal data is shown by the square symbols with the dotted line). Using a model similar to that of Takahashi et al. (which is shown in the temperature profile panel only – by the square symbols with dashed-line error bars) we also obtain the radially increasing temperature profile in the uncorrected convolved data (dashed line, triangle symbols). This last profile (solid line with diamond symbols) shows the recovery of the isothermal profile from the convolved data using our *SID* procedure. (See Fig. 6 for other plot details.)

[†] The nominal fraction of the total number of background-subtracted counts per annulus is 0.1, the soft-limit on the minimum number of counts in an annulus is 1,000 and the hard-limit is 500 counts.

[§] Our specific model is that of a single MEKAL thermal component (*i.e.* Mewe, Gronenschild, & van den Oord 1985; Mewe, Lemen, & van den Oord 1986), absorbed (Morrison & McCammon 1983) by a foreground column density of foreground material.

ground added) the convolved and deconvolved results are subject to extra noise which is not in the original dataset spectral fits.

4 CLUSTER SIMULATION RESULTS

4.1 Takahashi et al. Model – The Effect Of The PSF On ASCA Cluster Data

In the Introduction we referred to a paper by (Takahashi et al. 1995) which showed that the energy-dependent PSF of ASCA can give rise to an apparently increasing temperature profile in an isothermal cluster, if the data were not corrected for the effect of the PSF. Before we discuss our various simulation results, where we investigate different observational and physical scenarios, we show that we can reproduce this systematic effect when using similar parameters. (The magnitude of the effect depends on parameters, such as apparent size of the cluster core.)

As the effect of the PSF becomes severer for hotter clusters, we chose to approximate the hottest temperature profile modeled by Takahashi et al. (1995). We do this using a single β -model with a velocity dispersion of $1,100 \text{ km s}^{-1}$ (which with the $\beta_{\text{spec}} = 0.8$ which we use in our other models gives a central temperature of approximately $9 - 10 \text{ keV}$), an index for the profile of $\beta_{\text{fit}} = 0.6$ and a core radius of $R_{\text{core}} = 0.13 \text{ Mpc}$ (resulting in a 1 arcmin core, similar to Takahashi et al.). Further details of the parameters used are given in Table 1 under the *TEST-GCF-30K* model.

In Fig. 5 the effect of the PSF can be seen in the convolved dataset's temperature profile (dashed line with triangle symbols), where the temperature in the core is low and then it gradually increases with radius. This trend is similar to the Takahashi et al. profile, which we present in the plot as square symbols with dashed error-bar lines. The diagram also shows that our *SID* method recovers the true radial temperature, metallicity and emissivity profiles from the convolved data.

In the following tests we create a suite of models to investigate the effects of various observational and physical conditions on the ability of the *SID* procedure to recover the true intracluster gas properties.

4.2 Standard Test – A Cluster With A Strong Core Temperature Decline

With our basic prescription for creating a simulated cluster dataset (see Section 3.1), we choose our standard model to represent a 'Giant Cooling Flow' (*TEST-GCF-30K*). The variation in the average temperature in this type of cluster is expected to be significant, and will therefore provide a severe test for the *SID* procedure. To produce a core temperature decline we add a second cooler thermal component to the core region. Although this is not a physically realistic representation of a cooling flow it mimics a core temperature drop (albeit rather sharply) which is seen in typical cooling flow clusters (e.g. Centaurus – Allen & Fabian 1994). (Remember, we are not necessarily interested in the physical correctness of our model but whether the *SID* recovers the intrinsic energy and spatial distribution of the simulated cluster – whatever that might be.)

The parameters have been chosen to approximate the physical

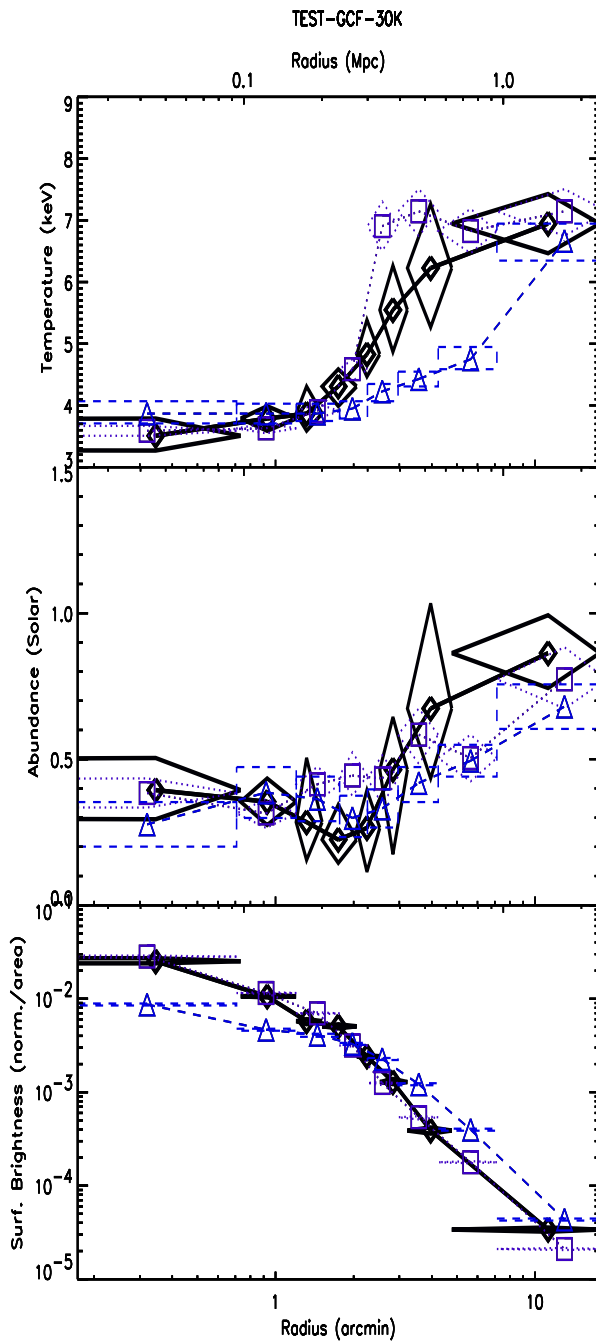


Figure 6. In this figure we plot the radial variations of electron temperature, metallicity (fraction of Solar), and model normalisation (i.e. emission measure: $10^{14}/(4\pi D_L^2) \int n_e n_H dV$) for a single thermal (MEKAL) component fit to the standard model (*TEST-GCF-30K*; see Section 4). The results for the deconvolved data are shown by the solid line, the convolved data by the dashed line, and the original data by the dotted line. The error bars on the temperature, abundance and normalisation are one standard deviation, while those on the x-axis data show the radial extent.

Test Name	Comments	Systematic/Instrumental Flags				Cluster Component					Fig. Ref.
		Bgd.	Pos.	Exp.	N_{IT}	T_X'	$\Delta N_{\text{H}}''$	T_X''	R_{core}''	R''_{max}	
<i>TEST-TAK-30K</i>	Takahashi et al. model	Yes	4.5	30	50	9.87	N/A	N/A	N/A	N/A	5
<i>TEST-GCF-30K</i>	'Standard' model	Yes	4.5	30	50	6.61	6.8	1.65	0.2	0.3	6
<i>TEST-MCF-30K</i>	Smaller cooling flow effect	3.31	7(a)
<i>TEST-ISO-30K</i>	Isothermal	N/A	N/A	N/A	N/A	7(b)
<i>TEST-DTX-30K</i>	Temperature decline	1.65	0	6.61	0.8	5	7(c)
<i>TEST-NOBGD-30K</i>	No background	No	8
<i>TEST-GCF-15K</i>	Short exposure	15	9(a)
<i>TEST-GCF-60K</i>	Long exposure	60	9(c)
<i>TEST-NIT25-30K</i>	Less image deconv. iterations	25	10(a)
<i>TEST-NIT150-30K</i>	More image deconv. iterations	150	10(b)
<i>TEST-OFF-30K</i>	Off-axis cluster	..	9.0	11(b)

Table 1. Variable Parameters For Generating Simulated Clusters

In all but the single-phase temperature model (*TEST-ISO-30*), there are two gas phases, as indicated by the primary and secondary superscripts. The model components which are inapplicable (*i.e.* the *TEST-ISO-30K* test) are indicated as such by 'N/A'. Entries with '..' indicate the values default back to the 'standard model': *TEST-GCF-30K*. Parameters which are invariant between each test are: (i) the total column density (*i.e.* Galactic; acting on both components where applicable): $1.36 \times 10^{21} \text{ cm}^{-2}$, (ii) redshift: 0.0881, (iii) baryon fraction: 0.1, (iv) β -parameter: 0.67, (v) abundance: $0.4Z_{\odot}$, (vi) velocity dispersion: 900 km s^{-1} (both components where applicable), (vii) core radius: 0.2 Mpc (primary component), and (viii) maximum radial extent: 5 Mpc (primary component). Each test is labelled to indicate the primary point in question. Those tests which investigate different cluster temperature profiles are: giant cooling flow: '*TEST-GCF-30K*', moderate cooling flow: '*TEST-MCF-30K*'; isothermal cluster: '*TEST-ISO-30K*'; radially decreasing temperature: '*TEST-DTX-30K*'. Those tests investigating instrumental/systematic effects are: inclusion of cosmic background '*TEST-NOBGD-30K*'; off-axis position '*TEST-OFF-30K*'; number of image-deconvolution iterations: '*TEST-NIT25-30K*' and '*TEST-NIT150-30K*'; exposure time (in kilo-seconds): '*TEST-GCF-15K*' and '*TEST-GCF-60K*'. The abbreviations for the systematic/instrument flags are as follows: 'Bgd.': background included; 'Pos.': off-axis position of the centre of the simulated cluster; 'Exp.': exposure duration; and ' N_{IT} ': number of iterations used in the M-L image deconvolution stage. The abbreviations for the cluster properties are: gas temperature ' T_X' '; excess absorption (only on second component): ' $\Delta N_{\text{H}}''$ '; core-radius: ' R_{core}'' '; and truncation maximum radius: ' R''_{max} '. Finally 'Fig.' indicates the figure reference for each test, while each test is discussed in Section 4.

characteristics of Abell 478. This is a cluster of moderate temperature, and distance, but is fairly luminous due to its large cooling flow. It should be remembered that some of the conclusions drawn from the following tests will be dependent on the characteristics of the cluster in question, *e.g.* whether the cluster has a cooling flow, or not, and how bright the cluster is, etcetera. Table 1 shows the parameters we have use in each test. The primary component has a temperature of 6.6 keV; the cooler component is at 1.65 keV, but its radial extent is truncated at $1.5 \times R_{\text{core}} = 0.3 \text{ Mpc}$ to limit it to the centre of the cluster. The cooler component spectrum is also modified by an additional column of absorbing material of five times the assumed Galactic value (which is set at $1.36 \times 10^{21} \text{ cm}^{-2}$) to model excess absorption (*i.e.* White et al. 1991 and Johnstone et al. 1992). For this standard model, the observational characteristics are an exposure of 30 ks, with the centre of the cluster placed 4.5 arcmin off axis (fairly standard for an *ASCA* GIS observation), and the data are convolved using a spatially varying PSF. (The PSF is interpolated from the grid of 11 different positions for the PSF in each energy band, supplied in the CALDB.)

The effect of the spectral-image deconvolution on the convolved data becomes apparent when we look at the radial variations in the spectral fit parameters in Fig. 6. This figure shows that the variations of the original ICM properties are recovered by the *SID*, and are a much better representation of the original variations than those obtained from the convolved data. (If a hydrostatic mass determination were made from the convolved data on such a cluster, then careful consideration of the complications would be re-

quired, if meaningful results were to be obtained.) We note, however, that the abruptness of the temperature profile decline in the original data, which is rather artificial due to the construct of our model, is somewhat smoothed over in the deconvolved temperature profile.

4.3 A Variety Of Different Temperature Profiles

In the next three tests we have attempted to span a wide range of possible temperature profiles. With the 'Medium Cooling Flow' model, *TEST-MCF-30K*, we investigate whether a less dramatic temperature decline can be recovered. In this case, the simulated data were created by adding a secondary component which is slightly hotter, *i.e.* 3.3 keV, than in the previous model. Figure 7(a) shows that the small differences between the original and convolved temperature profiles are still resolved with the deconvolved data.

In the *TEST-ISO-30K* model, Fig. 7(b), we eliminate the second cooler component altogether, and produce an isothermal temperature profile. This test shows that the deconvolution procedure essentially has no systematic effects which severely distort the recovery of a flat temperature profile and, for example, results in a temperature decline.

In the last temperature profile variation, *TEST-DTX-30K* – shown in Fig. 7(c), we have created a temperature profile which decreases radially outwards, to approximate the general trend for

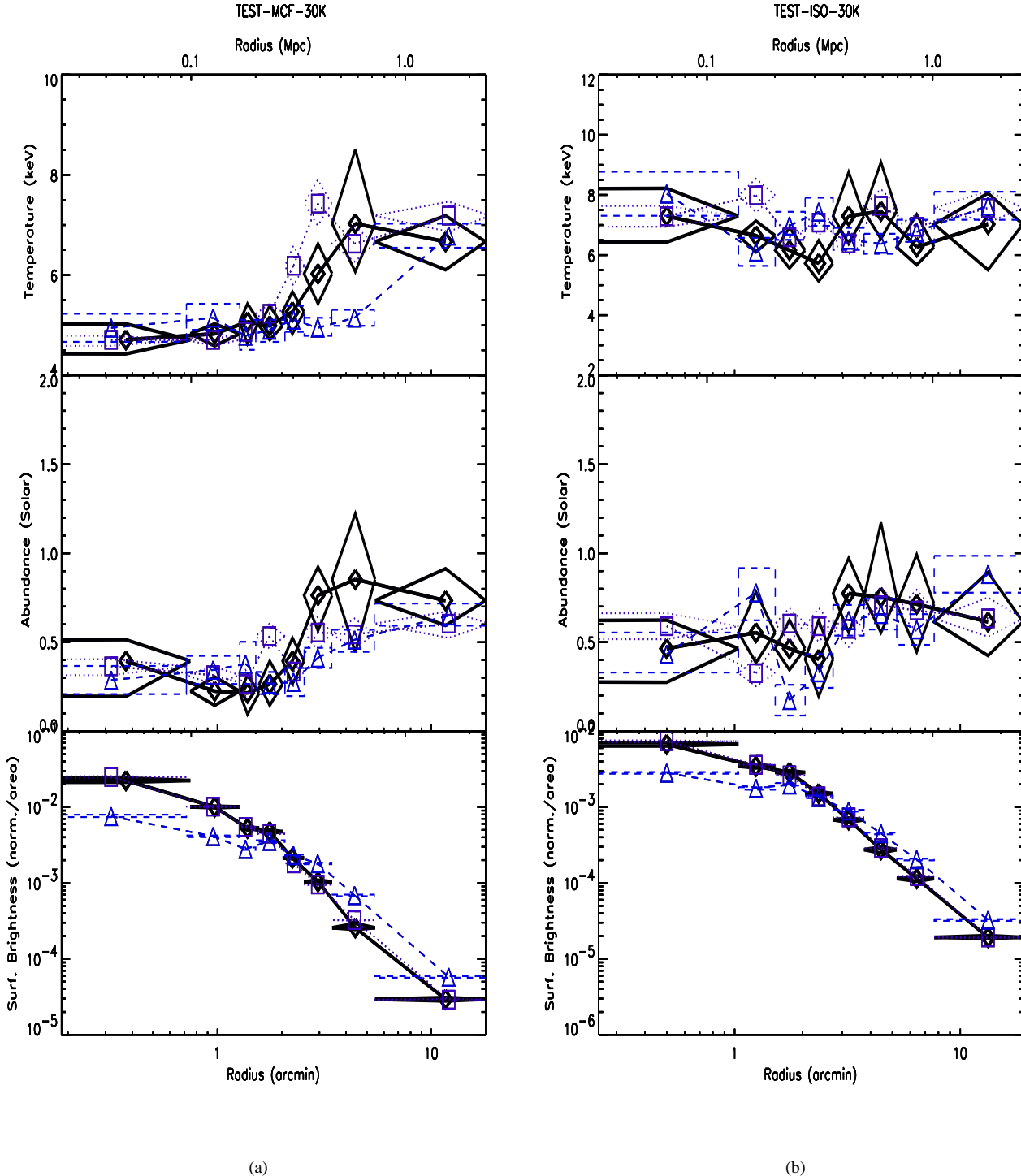
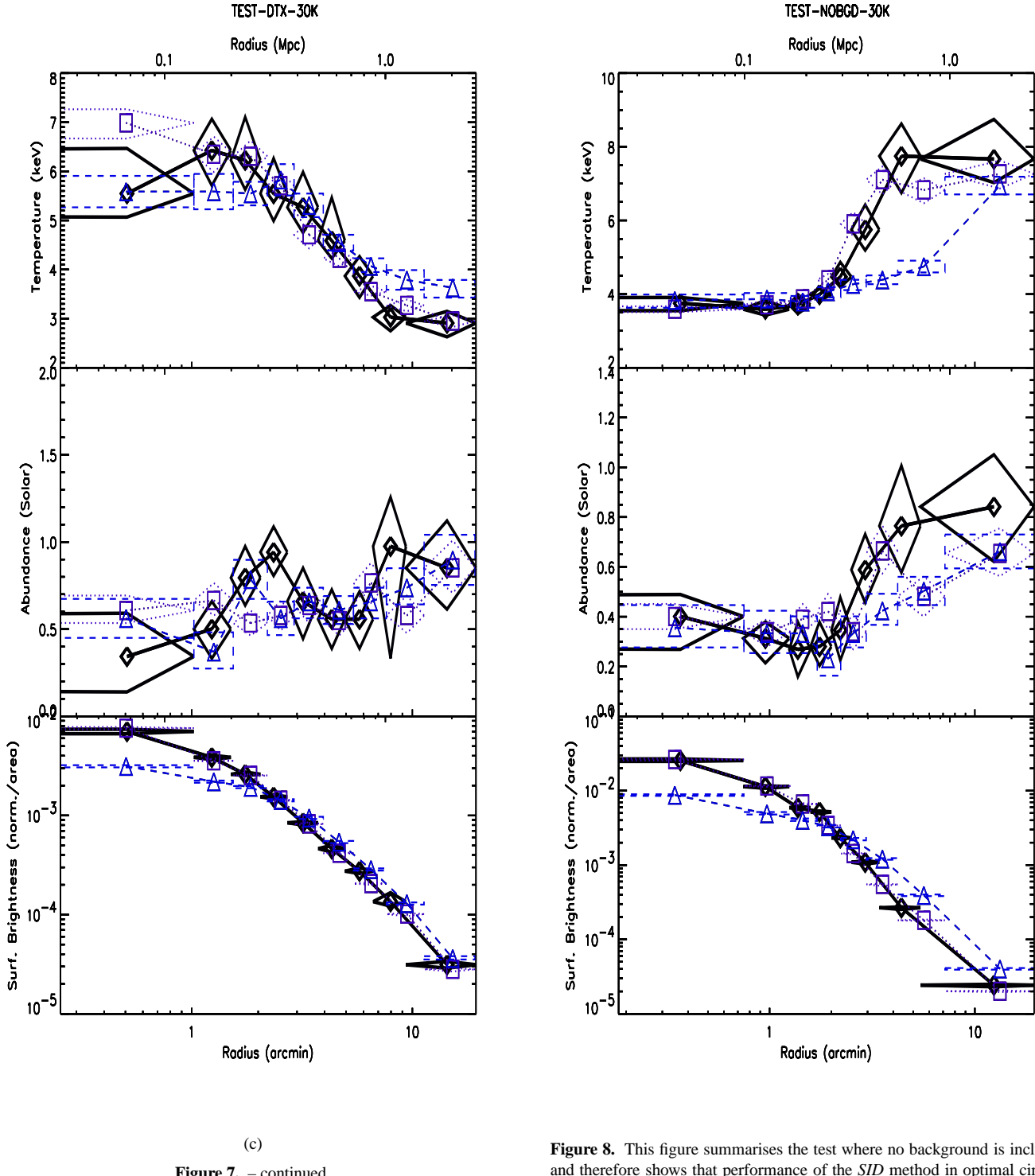


Figure 7. This figure summarises the tests of differing temperature profiles, as follows: (a) moderate core temperature drop, (b) and isothermal temperature profile, and (c) and temperature decline with radius. The line styles etc. are the same as those defined in Fig. 6.

decreasing temperature profiles found by *MFSV*. This model was created by making the hotter component more extended (*i.e.* the core-radius is larger), than the cool component (note, the truncation is set at 5 Mpc for both components and there is no excess absorption on the cooler emission component). Although the difference between the original and convolved temperature determinations in any particular radial bin is small, the general slope of the original profile is more accurately reproduced by the deconvolved data.

Despite the lower count rates from the *TEST-MCF-30K*, *TEST-ISO-30K* models, as they incorporate less flux from the secondary temperature component, these results show that the success of the deconvolution does not appear to be dependent on the intrinsic temperature variations, and that there are no severe systematic biases in the deconvolved profiles.

**Figure 7.** – continued.

4.4 Statistical Effects Due To Background And Exposure

We now turn our investigation to the impact of the various instrumental and systematic effects which occur in *ASCA* observations of clusters: the effect of background event contamination, and the impact of signal-to-noise variations.

In *TEST-NOBGD-30K* we see the intrinsic ability of the *SID* procedure in the absence of any background contamination. The

Figure 8. This figure summarises the test where no background is included, and therefore shows that performance of the *SID* method in optimal circumstances.

results are clearly more accurate, but are still qualitatively similar to the results from the standard simulation data which includes the background. This shows that performance of the *SID* procedure is relatively unaffected by background noise, at the expected level.

In Figs. 9 we show the effect of variations in data quality, using exposure times of 15 and 60 k s, *i.e.* factors of a half and twice the standard exposure (*TEST-GCF-15K* and *TEST-GCF-60K*). These models include the cosmic background, and therefore the reduction

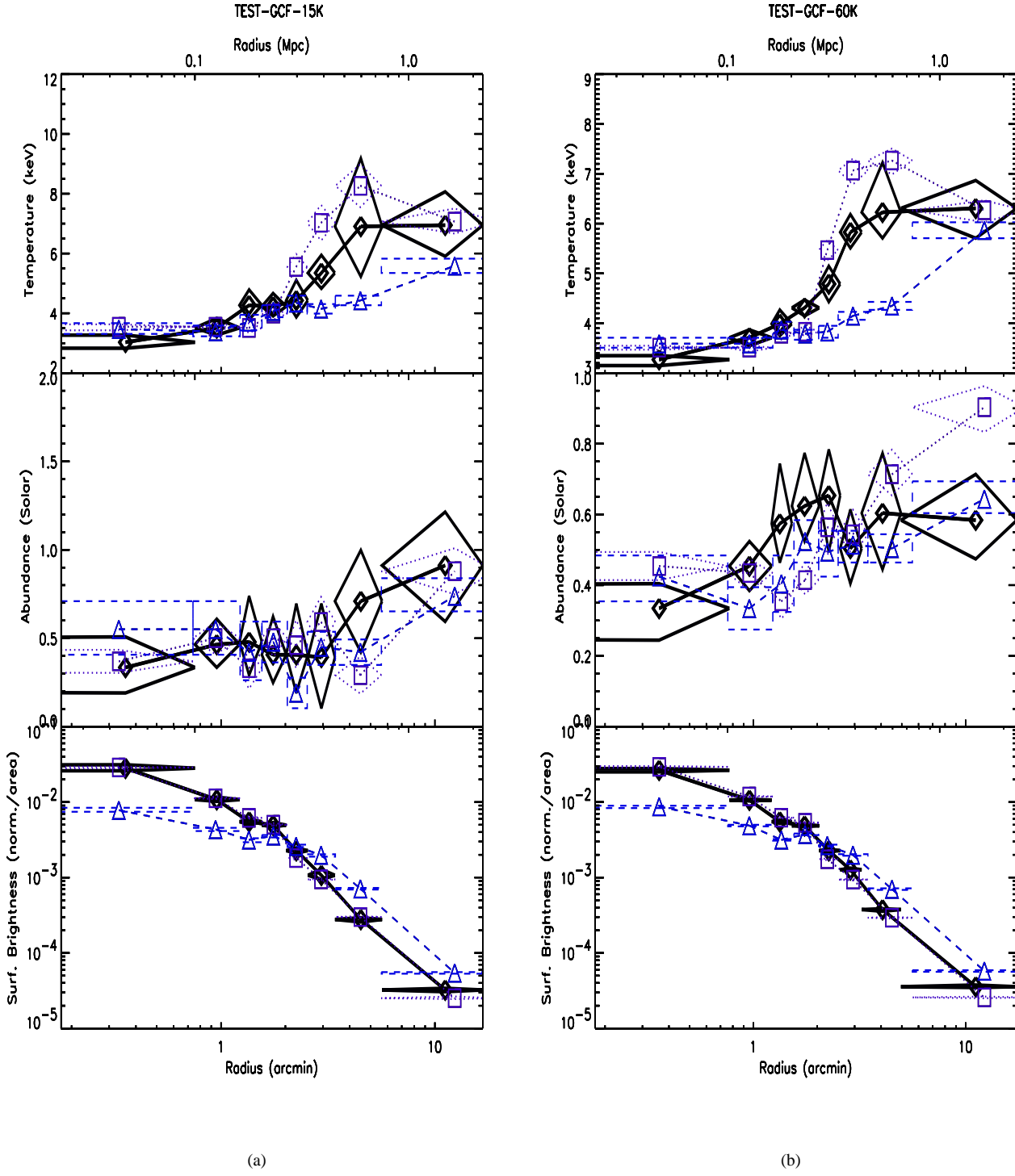


Figure 9. This figure summarises the test which investigates the effect of signal-to-noise through different exposures [(a): 15 and (b): 60 k s, *i.e.* a factor of one-half and twice the standard test's exposure].

in exposure time also results in a degradation of the signal-to-noise ratio.

In both cases the deconvolved temperature and emissivity profiles form much better representations of the original data than the convolved data. (The performance will, of course, differ for clusters with differing count distributions *i.e.* surface-brightness profiles, and count rates, *i.e.* signal-to-noise for a given exposure.)

4.5 Systematic Effects From Our Procedure

In Section 2.3 we discussed the Monte-Carlo technique which we have used to average-out systematic variations which occur in a single run of the SID procedure. We now discuss some potential sources for these systematic effects.

The primary assumptions in our procedure are that we can use

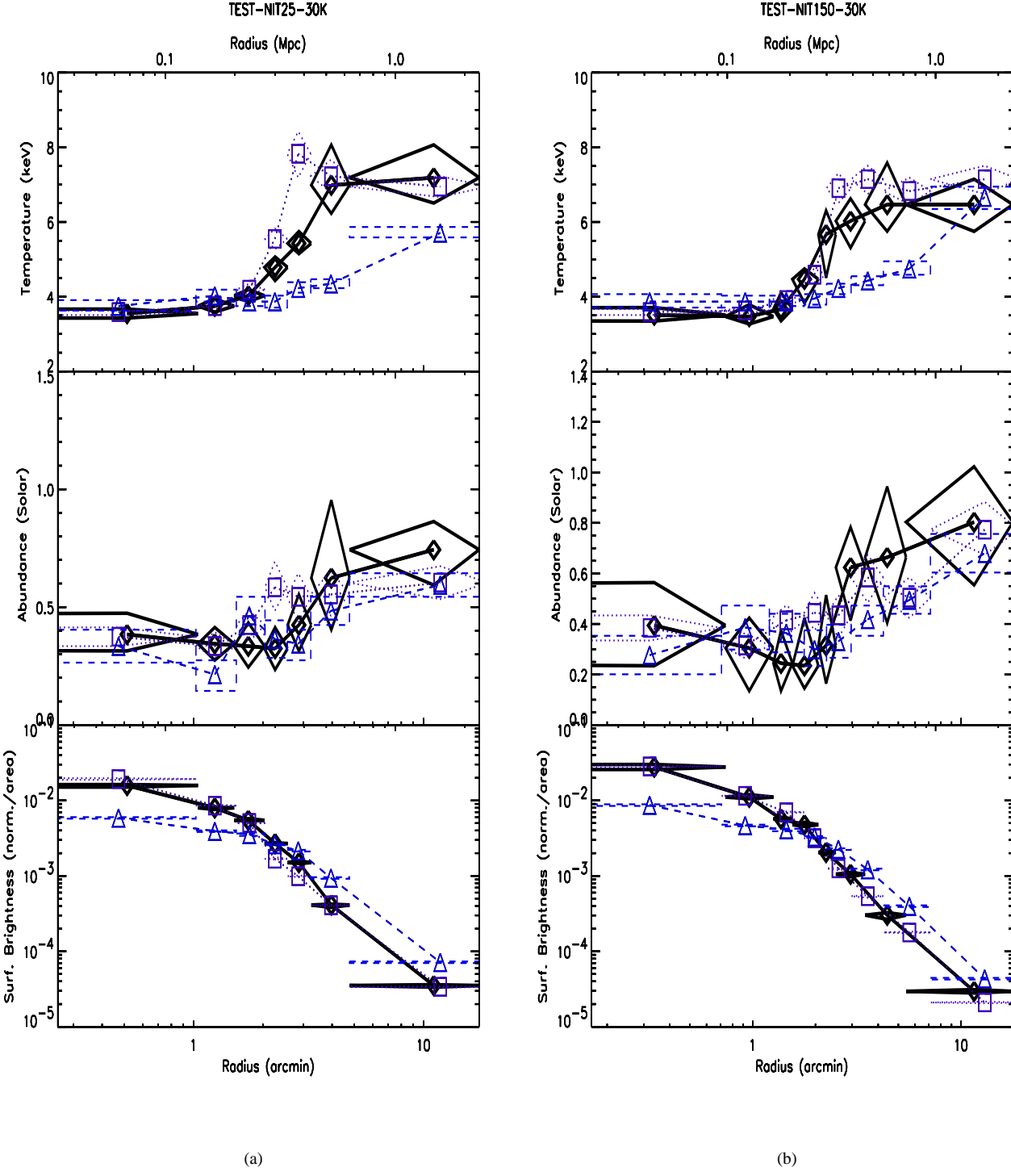


Figure 10. This figure summarises the tests which utilize fewer (25) or greater (150) number of iterations in the M-L stage of the image deconvolution, compared to the standard number of 50.

a spatially invariant PSF for the image deconvolution phase, and that the PSF is invariant across each 1 keV energy band for the spectral-reassignment. Before we investigate these issues we will look at the effect of varying the number of iterations employed in the image deconvolution phase of the *SID* procedure.

4.5.1 The Number of Image Deconvolution Iterations

In the *TEST-NIT-25* and *TEST-NIT-150* tests we vary the number of iterations employed in the (M-L) image deconvolution stage of the *SID* procedure from the standard number of 50, to 25 and 150 iterations, respectively. Figures 10(a) and 10(b) essentially show that the results are similar regardless of the number of iterations. A

greater number of iterations will produce sharper features, and thus follow the sharp temperature decline in the cooling flow models, but this will also exaggerate spurious features (although this will be minimised by the 10 Monte-Carlo runs of the *SID* procedure). For this particular cluster model, we find that 50 iterations appears to be optimal for recovering of the core temperature decline without introducing severe systematic effects into the abundance profile.

4.5.2 The Assumption Of A Spatially Invariant PSF

In Section 2.1 we described the use of the Maximum-Likelihood procedure, which requires the use of a spatially invariant PSF. However, the real *ASCA* PSF varies significantly with position (*e.g.* see Fig. 2). Thus, we have created all our simulated data using a spatially varying PSF (interpolating from the CALDB sample of 11 different PSF positions), and then deconvolved using a *fixed* PSF which is appropriate for the position of the centre of the cluster in the detector image. All the results presented so far show that this is a reasonable assumption which does not severely compromise the *SID* results. This is because most of the cluster photons arise from the core region, and therefore the fixed PSF approximation we have chosen is acceptable.

Our assumption will be poorer for more extended clusters, and for clusters centred further off-axis because the PSF changes more rapidly with increasing displacement from the centre of the detector (mainly in symmetry – see Fig. 2). In the *TEST-OFF-30K* test we see the results for a cluster placed near the edge of the field of view (9 arcmin from the on-axis position). Although the (abundance profile in particular) results are worse than for the near on-axis results (*TEST-GCF-30K*) the essential trends of the true emissivity and temperature profiles are recovered. We emphasise that most real cluster observations occur at the on-axis position we have selected for our standard *TEST-GCF-30K* test.

4.5.3 The Assumption Of An Spatially Invariant PSF Within Each 1 Kev Energyband

The scatter of the PSF continually degrades with increasing photon energy. This means that for events at the upper end of the energy band we will be using a PSF which is too narrow, and for the lower energy data we will be using a PSF which is too wide. When the spectral-reassignment procedure determines a map of events between the *source-* and *image-plane* it will choose hard events which are too concentrated, and soft events which are too far away than would be correct. The precise effect of this is complicated and probably depends on the spatial distribution of events, but undoubtedly it will change the slope of the spectral distribution within each 1 keV energy band, resulting in a slight discontinuity between the boundaries of each energy band. Fortunately, statistical noise in the data will help obscure these discontinuities, and none are visible in the deconvolved spectrum of the central region of our test shown in Fig. 4(e).

In summary of all these tests, we believe that our procedure will provide accurate results under a wide-range of observational circumstances.

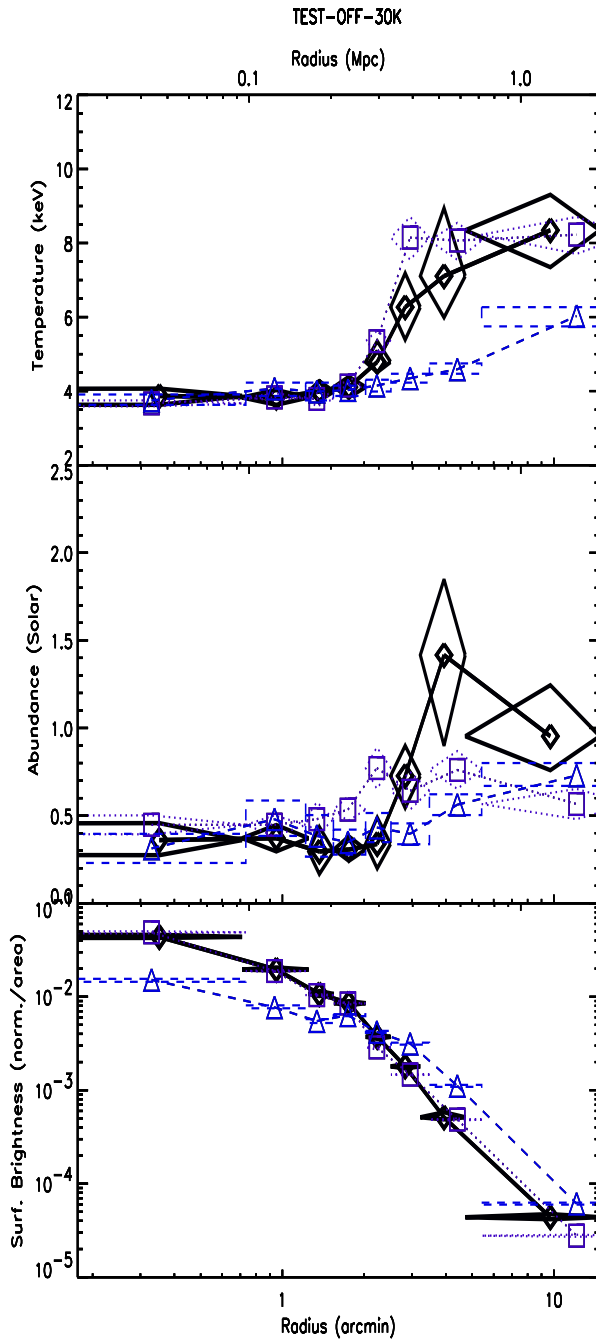


Figure 11. This figure shows the limitation of using the fixed-spatial PSF in the *SID* procedure when the cluster is positioned at a large (9 arcmin) off-axis angle.

5 CONCLUSIONS

In this paper we have presented a method for performing a spectral-imaging deconvolution analysis of X-ray data which has been affected by an energy- and position-dependent point-spread function (PSF), such as that produced by the *ASCA* satellite mirror arrangement. Without correction any spatially-resolved spectral analysis of *ASCA* data will be incorrect, as higher energy photons are scattered

further than lower energy photons. In studying spatially extended sources, such as clusters of galaxies, it is essential that a correction is made for this effect if accurate conclusion are to be drawn from the radial variations in the spectral properties of the object, *e.g.* the temperature and thereby mass profiles of galaxy clusters.

Markevitch et al. (1996) has presented a procedure which attempts to correct for the *ASCA* PSF, and in an analysis of 30 clusters Markevitch et al. (1998) found that virtually all their temperature profile results decrease with radius, according to an average polytropic index of $\gamma = 1.24^{+0.20}_{-0.12}$. If correct, this result is very important as it implies that clusters have less mass than would be assumed if they were isothermal, and thereby has implications for cosmology through cluster mass distributions and baryon fractions. However, the fact that the polytropic index is so steep, and close to the convective instability value of $\gamma = 5/3 = 1.67$, is of some concern as many clusters in their sample are cooling flows, and should therefore be relaxed clusters. It is therefore imperative that the *MFSV* results are verified by independent means.

We have developed an independent method which is self-contained, in that it does not require observational data on the same object from other X-ray satellites, or any assumption about the source spectrum. This means that potential systematic problems, arising from cross-calibration uncertainties, are eliminated. Also, unlike Markevitch et al., we present tests of our deconvolution procedure on realistic simulations of *ASCA* observations of clusters to show that our method successfully recovers the true radial properties of the intracluster gas from data under a wide variety of conditions. In particular, we have tested the recovery of differing intrinsic temperature profiles and we have included contamination from the observed cosmic and instrumental background of *ASCA*, to show that the procedure will work in practical application on reasonably bright clusters. We have also shown that the various limitations (*i.e.* were are forced to assume a spatially-invariant point-spread function) do not unduly compromise the ability of the procedure to successfully recover the original temperature profiles. All the deconvolved profiles we obtain are in good agreement with the true intrinsic properties.

In conclusion, our spectral-imaging deconvolution procedure is successful at recovering the original radial properties of the intracluster gas – for a range of different physical scenarios, and at the expected level of background and instrumental contamination. This procedure is, therefore, entirely capable of working in practical circumstances with observational data. In Paper-II (White 1999a) we apply this spectral-imaging deconvolution procedure to real *ASCA* data on 106 clusters, and compare the results with those from Markevitch et al. In Paper-III (White 1999b) we select a sub-sample of these objects for mass profile determinations.

6 ACKNOWLEDGEMENTS

D.A. White acknowledges support from the P.P.A.R.C.; D. Buote that of P.P.A.R.C. and by NASA through Chandra Fellowship grant PF8-10001 awarded by the Chandra Science Center, which is operated by the Smithsonian Astrophysical Observatory for NASA under contract NAS8-39073. We thank S.W. Allen and A.C. Fabian for useful discussion, and R.M. Johnstone for assistance.

This research has made use of data obtained through the High

Energy Astrophysics Science Archive Research Center Online Service, provided by the NASA/Goddard Space Flight Center.

The authors thank the anonymous referee for useful comments.

REFERENCES

- Allen S.W., Fabian A.C., 1994, MNRAS, 269, 409
 Arnaud K.A., 1996, in Jacoby G., Barnes J., eds, ASP Conf. Series volume 101. ASP Conf. Series volume 101., p. 17
 Briel U.G., Henry J.P., Böhringer H., 1992, A&A, 259, L31
 Buote D.A., 1998, 293, 381
 Buote D.A., Tsai J.C., 1996, ApJ, 458, 27
 Donnelly R.H., Markevitch M., Forman W.R., Jones C., David L.P., Churazov E., Gilfanov M., 1998, ApJ, 500, 138
 Ettori S., Fabian A.C., 1998, MNRAS, 293, L33
 Ezawa H., Fukazawa Y., Makashima K., Ohashi T., Takahara T., Xu H., Yamasaki N.Y., 1997, ApJ, 490, L36
 Fujita Y., Koyama K., Tsuru T., Matsumoto H., 1996, PASJ, 48, 191
 Henricksen M.J., Markevitch M., 1996, ApJ, 466, L79
 Ikebe Y. et al., 1997, ApJ, 481, 660
 Irwin J.A., Bregman J.N., Evrard A.E., 1998, ApJ, Vol. N/A, submitted
 Johnstone R.M., Fabian A.C., Edge A.C., Thomas P.A., 1992, MNRAS, 255, 431
 Markevitch M., 1996, ApJ, 465, L1
 Markevitch M., Forman W.R., Sarazin C.L., Vikhlinin A., 1998, ApJ, in press, astro-ph/9711289v2
 Markevitch M., Mushotzky R., Inoue H., Yamashita K., Furuzawa A., Tawara Y., 1996, ApJ, 456, L71
 Markevitch M., Sarazin C.L., Irwin J.A., 1996, ApJ, 472, L17
 Markevitch M., Vikhlinin A., 1997, ApJ, 474, 84
 Mewe R., Gronenschild E.H.B.M., Oord van den G.H.J., 1985, A&A, 62, 197
 Mewe R., Lemen J.R., Oord van den G.H.J., 1986, A&A, 65, 511
 Molendi S., Grandi S. De, Fusco-Femiano R., Colafrancesco S., Fiore F., Nesci R., Tamburelli F., 1999, ApJ, in press, astro-ph/9909228
 Morrison R., McCammon D., 1983, ApJ, 270, 119
 Ohashi T., Honda H., Ezawa H., Kikuchi K., 1997, in Makino F., Mitsuda K., eds, X-Ray Imaging and Spectroscopy of Cosmic Hot Plasmas. Universal Academy Press Inc., Tokyo, Japan, p. 49
 Sarazin C.L., Wise M.W., Markevitch M., 1998, ApJ, 498, 606
 Takahashi T., Markevitch M., Fukazawa Y., Ikebe Y., Ishisaki Y., Kikuchi K., Makashima K., Tawara Y., 1995, in ASCA Newsletter, (NASA/GSFC), Volume 3
 White D.A., 1999a, MNRAS, accepted, (Paper-II)
 White D.A., 1999b, MNRAS, in prep., (Paper-III)
 White D.A., Fabian A.C., 1995, MNRAS, 273, 72
 White D.A., Fabian A.C., Johnstone R.M., Mushotzky R.F., Arnaud K.A., 1991, MNRAS, 252, 72
 White S.D.M., Navarro J.F., Evrard A.E., Frenk C.S., 1993, Nat, 366, 429